Mechanical Rippling for Diverse Ferroelectric Topologies in Otherwise Nonferroelectric math xmlns="http://www.w3.org/1998/Math/MathML" display="inline">mrow>msub>mrow>mi>SrTiO/mi>/mrow>mn>3/mn>/msub>/mrow>/math> Nanofilms

Tao Xu, Chengsheng Wu, Sizheng Zheng, Yu Wang, Jie Wang, Hiroyuki Hirakata, Takayuki Kitamura, and Takahiro Shimada

Phys. Rev. Lett. **132**, 086801 — Published 21 February 2024

DOI: 10.1103/PhysRevLett.132.086801

Mechanical rippling for diverse ferroelectric topologies in otherwise nonferroelectric $SrTiO_3$ nanofilms

Tao Xu[1,2]*, Chengsheng Wu[1,5], Sizheng Zheng[3], Yu Wang[2], Jie Wang[3,4]*, Hiroyuki Hirakata[2], Takayuki Kitamura[2], Takahiro Shimada[2]

[1]*Ningbo Institute of Materials Technology and Engineering, Chinese Academy of Sciences, Ningbo 315201, China*
[2]*Department of Mechanical Engineering and Science, Kyoto University, Nishikyo-ku, Kyoto 615-8540, Japan*
[3]*Department of Engineering Mechanics, School of Aeronautics and Astronautics Zhejiang University, Hangzhou 310027, China*
[4]*Zhejiang Laboratory, Hangzhou 311100, Zhejiang, China*
[5]*College of Materials Science and Engineering, Zhejiang University of Technology, Hangzhou 310014, China*

Abstract

Polar topological structures such as skyrmions and merons have become an emerging research field due to their rich functionalities and promising applications in information storage. Up to now, the obtained polar topological structures are restricted to a few limited ferroelectrics with complex heterostructures, limiting their large-scale practical applications. Here, we circumvent this limitation by utilizing a nanoscale ripple-generated flexoelectric field as a universal means to create rich polar topological configurations in nonpolar nanofilms in a controllable fashion. Our extensive phase-field simulations show that a rippled $SrTiO_3$ nanofilm with a single bulge activates polarizations that are stabilized in meron configurations, which further undergo topological transitions to Néel-type and Bloch-type skyrmions upon varying the geometries. The formation of these topologies originates from the curvature-dependent flexoelectric field, which extends beyond the common mechanism of geometric confinement that requires harsh energy conditions and strict temperature ranges. We further

demonstrate that the rippled nanofilm with three-dimensional ripples patterns can accommodate other unreported modulated phases of ferroelectric topologies, which provide ferroelectric analogs to the complex spin topologies in magnets. The present study not only unveils the intriguing nanoscale electromechanical properties but also opens exciting opportunities to design various functional topological phenomena in flexible materials.

Main text

Topological defects in ferroics, such as skyrmions and merons, have attracted enormous attention recently due to their rich physical phenomena, new functionalities, and promising potential applications in next-generation electronic devices [1-3]. The formation of such topological textures has been widely explored in ferromagnetism with noncollinear spin interactions (e.g., Dzyaloshinskii-Moriya interactions (DMI) [4-6]). Despite the absence of such intrinsic noncollinear interactions, many nontrivial polar topological structures that are well known in ferromagnets have also been predicted and verified recently in ferroelectric nanocomposites and ferroelectric/paraelectric superlattices, such as flux-closure domains [7, 8], vortices[9,10], polar skyrmions [11,12] and merons [13,14], which provide a new paradigm for high-density and ultralow-power-consumption nanoelectronic devices. While such explorations are illuminative, the occurrence of polar topological structures in low-dimensional structures and oxide superlattices is limited to very few ferroelectrics and relies on the harsh energy conditions among elastic, electrostatic and gradient energy, limiting their large-scale practical applications. Exploring a simple yet general scheme for the generation of polar topological structures is thus of great interest and demand.

Recently, the exploitation of charged impurity defects that are associated with strong

electrochemo-mechanical interactions seems to be a promising avenue to discover exotic polarization patterns, such as vortices [15] and hedgehog polarization [16]. Such defect-mediated electromechanical properties have also been utilized in $SrTiO_3$ heterostructures to break the lattice symmetry locally, recently leading to rich polar topological structures and transitions [3]. Nevertheless, defects can cause adverse effects on the performance of perovskite oxide-based devices, and precise control of defects is quite challenging. Strain engineering is another widely investigated means to systematically modulate a range of structural, electronic, and ferroelectric properties of perovskite oxides. In addition to applying a homogenous strain field, a strain gradient is also coupled to electric polarization, leading to a higher-order electromechanical coupling effect referred to as the flexoelectric effect [17-50]. The flexoelectric effect is ubiquitous in all dielectric materials due to the inversion symmetry-breaking induced by the strain gradient, which becomes significantly prominent at the nanoscale where the strain gradients are more intense. In particular, the nontrivial role of flexoelectricity in the generation of polar vortices has been quantified recently [20]. The strain gradient near the crack tip of $SrTiO_3$ has also been demonstrated to provide the driving force for the mechanical design of a variety of nontrivial polar structures [21], which suggests that flexoelectric effects could play a role in noncollinear interactions similar to DMI. Moreover, evoked by recent realizations of freestanding ultrathin perovskite oxides with excellent mechanical flexibility [22,23], wrinkled ferroelectric oxide members with finely controlled patterns have been designed and fabricated in experiments to explore distinct and enhanced functionalities [24,25]. In these wrinkled two-dimensional perovskite oxides, the local strain distributions change on the scale of the crystal lattices, and thus, the flexoelectric effects can be quite significant or even dominant due to the large strain gradients (10^6~10^9 m^{-1}) [26] that far exceed those in bulk phases.

In this work, we reveal that a rich variety of ferroelectric patterns with controllable topologies can be mechanically excited and designed by rippling morphologies in otherwise nonferroelectric $SrTiO_3$ nanofilms. The critical role of flexoelectricity in the generation of these complex polarizations is highlighted, which is unique with respect to the common mechanism by exploiting complicated nanostructures to achieve delicate energy balance. The proposed strategy of engineering rippling at the nanoscale provides a fertile platform for the exploration of diverse unknown polar textures in a wide range of materials, which could facilitate the development of novel flexible nanoelectronics.

Phase-field simulations are conducted to investigate the ferroelectric properties and domain patterns in the rippled $SrTiO_3$ thin film. The temporal evolution of polarizations is described by the time-dependent Ginzburg-Landau equation as

$$\frac{\partial P_i(\mathbf{r},t)}{\partial t} = -L\frac{\delta F}{\delta P_i(\mathbf{r},t)} \quad (1)$$

in which $P_i(\mathbf{r},t)$ is polarization, L is the kinetic constant and $F=\int_V f\,dV$ denotes the system's total free energy. The energy density f of the system consists of Landau, gradient, electrostatic, elastic and flexoelectric ones (see Supplemental Material [27]). In addition, the mechanical equilibrium equation, $(\sigma_{ij} - t_{ijk,j})_{,i} = 0$, and electric equilibrium equation, $D_{i,i} = 0$, are solved simultaneously, where σ_{ij} is the stress component, t_{ijk} is higher order stress and D_i is the electric displacement component. Periodic boundary conditions are employed along the [100] and [010] directions, and the open-current electric boundary condition is applied to the top and bottom surfaces. Inspired by the fabrication of wrinkled ferroelectric oxide members with excellent flexibility and finely controlled patterns, we consider diversified ordered wrinkling patterns for the $SrTiO_3$ nanofilm, including a single bulge, and periodic sinusoidal, herringbone and checkboard patterns, to demonstrate the design concept of mechanical rippling for polar topological structures. Details of the loading methods of these wrinkling patterns are

provided in Supplemental Material [27]. These deformation patterns are endowed with complex strain distributions and are typical ones that have been either proposed theoretically [37-39] or previously demonstrated through different fabrication methods and experimental processes [24,25,40-42].

We begin with the exploration of possible domain patterns in a nanofilm with a single bulge as a representative of isolated nanoscale deformation for its simplicity. Such nanoscale buckling structures can be easily triggered by various energy dissipations, such as stress fields and thermal fluctuations. As illustrated in Figure 1(a) for the simulation model, the geometry of the nanofilm is set to 30 nm × 30 nm × 3 nm, and a spherical bulge with a buckling height ω of 0.2 nm within a diameter of 12 nm is located in the center of the nanofilm. Although $SrTiO_3$ is intrinsically paraelectric, the wrinkling of the nanofilm induces nonzero electric polarization within the bulge. As illustrated in Figure 1(b) for the cross-sectional view of the polarization distribution, the out-of-plane polarization P_3 is dominant in the center of the bulge despite the decreasing values close to the surface due to a strong depolarization field, while the in-plane component is mainly distributed in the peripheral region of the bulge, which is more prominent near the surface layers. Consequently, the polarization distributions of the top (Z = 3 nm) and bottom (Z = 0 nm) layers show trivial in-plane configurations (see Figure S1).

On the other hand, the polarization forms a three-dimensional ferroelectric texture for the subtop (Z = 2.5 nm) and subbottom (Z = 0.5 nm) layers. Their in-plane views (x-y plane) of the polarization distribution within the bulge are illustrated in Figure 1(c) and (d), in which the arrows represent the polarization vectors and the color of the vectors denotes the out-of-plane component of polarization. The polarization is characterized by a radial symmetry distribution, with P_3 dominating in the center and comparable in-plane components P_1 and P_2 emerging near the peripheries in both layers. For the subtop layer, the polarization vectors in the core region point upward with a magnitude of

approximately 3.9 μC/cm^2 and gradually rotate and change into in-plane directions near the peripheries, which adopt a hedgehog-type distribution and feature a center divergent polar meron, while those in the subbottom layer consist of central-up polarizations with a magnitude of approximately 3.3 μC/cm^2 and inward radial in-plane polarizations, manifesting as a center convergent meron. Such a Neel-type polar meron is characterized mathematically by the topological number Q defined by

$$Q = \iint \frac{1}{4\pi} \boldsymbol{u} \cdot \left(\frac{\partial \boldsymbol{u}}{\partial x} \times \frac{\partial \boldsymbol{u}}{\partial y} \right) dxdy, \qquad (2)$$

where $\boldsymbol{u}$ is the normalized polarization vector. The obtained topological number is approximately 0.5, which demonstrates that they are indeed topological merons. The polar meron is more stable than other non-topological configurations, as discussed in section 2 of the Supplemental Material [27]. The corresponding topological density distributions q, i.e., the integrand of Eq. (2), are also plotted in Figure S2(a) and (b) for clarity, in which the largest value of approximately 0.07 nm^{-2} emerges in the center and periphery of the meron. As the simulation temperature rises to 300 K, the emerged polar merons remain unaffected (see Figure S3).

To elucidate the origins of the meron, we investigate the morphology-induced strain distribution in the nanofilm. Figure S4 illustrates the contour plots of the in-plane and out-of-plane distributions of different strain components. The rippling deformation causes in-plane expansion and shrinkage on the upper and lower layers around the center of the bulge, resulting in tensile and compressive strain zones for the upper and lower layers, respectively (Figure S4(a)). This strain variation from top to bottom induces a large strain gradient $\varepsilon_{11,3}$ and $\varepsilon_{22,3}$ of 2.1×10^7 m^{-1}. Comparable strain gradients were also obtained in recent experiments in wrinkled ferroelectric oxides [25] or by an atomic force microscope tip [43]. In addition, the in-plane deformation is also nonuniform within the same x-y plane. As illustrated in Figure S4(b) for the results of the x-y plane with Z = 2.5 nm as an example, the inner and

periphery of the bugle are subjected to opposite strains, i.e., ε_{11} and ε_{22} are positive in the center and the values become negative outside, which also results in considerable strain gradients $\varepsilon_{11,1}$ and $\varepsilon_{22,2}$ within the plane. Similarly, other components of strain gradients are also created along the thickness direction of the nanofilm or within the plane. As a result, these nanoscale spatially varying strain gradient fields contribute to the flexoelectric field $\mathbf{E}^f$, defined as $E_i^f = f_{jkil}\varepsilon_{jk,l}$. The flexoelectricity of the $SrTiO_3$ film consists of three components, i.e., longitudinal, transverse and shear coupling with coefficients f_{11}, f_{12} and f_{44}, respectively. As illustrated in Figure 2(b) and (d), flexoelectric fields E_1^f and E_2^f are mainly induced by the longitudinal (i.e.,$\varepsilon_{11,1}$ and $\varepsilon_{22,2}$) and shear flexoelectric components, which are antisymmetric about the x_2 and x_1 axes, respectively. These flexoelectric fields contribute to the in-plane polarizations with an outward radial pattern (see Figure 2(a) and (c)). Moreover, the flexoelectric field E_3^f (see Figure 2(f)) is mainly stimulated by transverse strain gradients (i.e., $\varepsilon_{11,3}$ and $\varepsilon_{22,3}$). The field value is largest in the center region and decreases radially, which contributes to the radially decreased out-of-plane polarization (see Figure 2(e)). The superposition of these comparable in-plane and out-of-plane polarizations originating from flexoelectric effects leads to the formation of nontrivial polarization in nonferroelectric $SrTiO_3$ nanofilms. This distribution is further confirmed by calculating the corresponding ferroelectric properties of the nanofilm in the absence of flexoelectricity (i.e., all flexoelectric coefficients are set to zero), which does not produce any polarization in the system. Therefore, the flexoelectric effect intrinsic to the rippling morphology imposes an electric field parallel to the radial direction of curvature and polarizes the otherwise nonpolar $SrTiO_3$. The curvature direction-dependent flexoelectric field performs the role of noncollinear interactions similar to those in ferromagnets for the formation of magnetic topological structures. Similar polar merons have also recently been reported in strained oxide ferroelectrics

despite their different origin mechanisms [14].

After clarifying the formation mechanism of the polar meron, the stability of the polar topological structures in the rippled $SrTiO_3$ is further investigated by changing the buckling height ω and thickness d of the thin film. The representative polar textures in the rippled nanofilm with different geometries are illustrated in Figure 3 and Figure S5 for the inner and surface layers, respectively. When the thickness d is increased to 7 nm with the same ω of 0.2 nm, the polarization distributions of the surface layers keep the in-plane configuration, while the domain pattern evolves from a polar meron to a Néel -type polar skyrmion in the inner layers with Z = 4.5 nm and 2 nm (Figure 3(a) and (b)). Upon further increasing ω from 0.2 nm to 2.0 nm, Bloch-type skyrmion emerges in the nanofilm (Z = 4.5 nm and 2 nm), as illustrated in Figure 3(c) and (d). The strain analysis shows that these topological phase transitions arise from a considerable change in the strain gradient distribution due to the modification of the geometries, which generates negative E_3^f, downward polarization in the center (see Figure S6) and resulting skyrmions in these layers. Moreover, we also note that the electrical boundary conditions have significant effects on the polarization configuration of ferroelectric materials. In this case, we further investigate the polarization configuration of the same deformed nanofilm under short-circuit conditions. As illustrated in Figure S5(e) and (f), the suppressed out-of-plane polarization increases dramatically due to the decrease of depolarization field, and a three-dimensional polarization texture emerges even in the surface layers. This result indicates that a perfect polar meron can also be created at the surface by properly adjusting the depolarization field. Furthermore, by applying external electric fields of 10 MV/m along $[00\bar{1}]$ (see Figure 3(e)(f) and Figure S5(g)(h)), these configurations transform into center-divergent and center-convergent skyrmions for the upper (Z = 3 nm and 2.5 nm) and lower (Z = 0 nm and 0.5 nm) layers, respectively. All these results indicate that rich topological transitions

can be achieved in the deformed $SrTiO_3$ nanofilm through modification of the geometry of the nanofilm (i.e., strain gradient) or electrical boundary conditions.

Since more complex deformations can be easily introduced into the nanofilm in practice, the strategy of rippling morphology control may provide the possibility to design various polar textures. We then investigate the periodic wrinkled $SrTiO_3$ thin film with a one-dimensional sinusoidally alternating peak and valley morphology, as illustrated in Figure 4(a). As expected, nonzero polarization also emerges in the $SrTiO_3$ nanofilm. The polarization forms tail-to-tail and head-to-head domain patterns along the *x* direction for the surface layers (see Figure S7(b) and (c)). Note that these domain walls are typically charged and are stabilized by compensating free carriers. Despite the absence of free carriers in our models, the flexoelectric field E_1^f stabilizes these head-to-head and tail-to-tail domain walls through a gradual variation in electric polarization. On the other hand, strip domain structures are observed between periodic peak and valley regions for the inner layers with Z = 2 nm and 1 nm (see Figure 4(b) and Figure S7(d)). In the layer with Z = 2 nm, the peak surface with positive curvature possesses upward [001] polarization, and the polarization spreads away from the center and gradually changes into in-plane directions in the neutral region. These polarizations continue to rotate and converge to opposite $[00\bar{1}]$ directions in the valley surface with negative curvature. As a result, the obtained stripe domain pattern is characterized by tail-to-tail center-divergent and head-to-head center-convergent domain walls, which are located in the peak and valley regions, respectively. The lower layer with Z = 1 nm possesses similar domain structure characteristics but the opposite direction of in-plane polarization. These configurations are reminiscent of the striped domain with Neel-type domain walls in ferromagnetics that arise from the competition of exchange coupling energy and DMI energy. The emerged polar stripe domain arises from the superposition of P_1 and P_3 components

originating from the wrinkling-induced robust nanoscale flexoelectric fields: the pseudoelectric field E_3^f is primarily generated at the sites of peaks and valleys of the wrinkles where the largest deformation exists, while E_1^f dominates the pseudoelectric field at the neutral regions (see Figure S8).

A $SrTiO_3$ thin film with a 2D herringbone wrinkle morphology is also considered, as illustrated in Figure 4(c) and (d). It is evident that out-of-plane polarization dominates in the peak and valley areas showing twisted stripe patterns, while the largest in-plane components appear in the neutral layer. The total electric polarization from the superposition of these components rotates continuously at the peak and valley areas along [100], forming a stripe domain with periodic tail-to-tail center-divergent and head-to-head center-convergent domains. In addition, the total electric polarization vector also shows the second sinusoidal ordering along the [010] direction, coinciding with the rippling morphology periodicity. Therefore, the polarization pattern is characterized by two perpendicular modulations described by two vectors, which jointly determine the periodicity of the polar pattern and lead to a labyrinth-like polarization pattern. A similar double-vector-modulated ferroelectric domain pattern has also been observed in ferroelectric-metallic superlattices very recently [44] due to the complicated coupling of interfacial oxygen octahedral tilt and surface dipoles. Nevertheless, our strategy provides a simpler physical mechanism yet more flexible approach to create a more complex ordered polarization pattern with coexisting modulation vectors.

Another surface morphological pattern that is commonly reported in experiments is the checkboard mode, which is a typical 2D ordered deformation pattern. An overview of the obtained polar pattern in the inner layers of this rippled nanofilm is shown in Figure 4(f) and Figure S7(l), and manifests as a polar meron-antimeron crystal that is characterized by a periodic square array of alternating core-up merons and core-down antimerons with a half-integer skyrmion number. The

polarization points upward and downward in the peak and valley, surrounded by in-plane polarization at the strain neutral regions. The Pontryagin density (see Figure S9) also exhibits square order, with the brightest regions corresponding to the cores of (anti)merons. Such a two-dimensional square (anti)meron lattice has recently been observed in chiral magnets [45]. Figure S10 illustrates the in-plane polarization components P_1 and P_2 and the out-of-plane component P_3, all of which feature round-shaped ordered pair patterns with opposite directions. These regularly distributed polarization components are related to the corresponding strain gradients (see Figure S11) associated with the rippling morphology. Moreover, all these topological structures show little change as temperature increase to 300 K, indicating their robust stability at room temperature.

The rippling morphologies discussed above can be qualitatively or even quantitatively manipulated by external stimuli such as mechanical loading [17,24,37,38,46], providing a voltage-free mechanism for exquisite material design and control over the properties and location of complex topological structures. In addition to the rippling morphologies investigated here, other complex self-assembled superstructures, such as origami, kirigami or even 3D twisting [47], were also reported, which provide more degrees of freedom for the modulation of the strain gradient and the resulting topological structures. Recently, the creation and control of rippled structures with various morphologies has also been reported in other thin films such as 2D materials [48-50], gels [51] and biological tissues [46], among which the flexoelectric coefficients in 2D materials have been widely investigated and predicted to be significant [53-55]. By virtue of its ubiquity, the rippling morphology-mediated flexoelectric field may universally engender intriguing polar topological structures in various functional materials that are intrinsically nonferroelectric materials via pure mechanical deformation. Moreover, intrinsic electric polarization in many classical ferroelectric materials is sensitive to

temperature and loses its ferroelectricity above the Curie temperature, which requires strict temperature conditions for the stabilization of polar topologies, while flexoelectrically induced polarization is temperature insensitive; thus, the activated polar topologies can be stabilized over a wide temperature range.

In summary, we have presented a new concept and approach for the creation of rich polar topological structures in nonpolar $SrTiO_3$ nanofilms, including meron, skyrmion, and meron-antimeron crystals, by purely mechanical rippling that are commonly observed in experiments or investigated in theory. The origin of these nontrivial topologies is related to curvature- and location-dependent strain gradients that generate noncollinear electric polarization via the temperature-independent flexoelectric effect, which is a completely different mechanism from the common case of requiring complex nanostructures and delicate energy interplay. Given the universality of flexoelectricity, our approach for polar topological structures is applicable to a wide range of nonpolar materials, thus providing a general and feasible pathway for the design and manipulation of innovative topological-based nanoelectronics.

ACKNOWLEDGMENTS

The work is supported by the National Natural Science Foundation of China (Grant Nos. 12172370, 12272338, 12192214), the National Key Research Development Program of China (No. 2022YFB3807601), Natural Science Foundation of Zhejiang Provincial (Grant Nos. LY22E020012), Natural Science Foundation of Ningbo City (Grant Nos. 2022J295), Zhejiang Laboratory Open Research Project (Grant No. K2022PE0AB06), JSPS KAKENHI (Grant Numbers JP23H00159, JP23K17720, JP20H05653), and JST FOREST Program (Grant Number JPMJFR222H), and JSPS International Research Fellow (No. P22065).

* E-mail: xutao@nimte.ac.cn; jw@zju.edu.cn

Reference

[1] S. Woo, K. Litzius, B. Krüger, M. Im, L. Caretta, K. Richter, M. Mann, A. Krone, R. Reeve, M. Weigand, P. Agrawal, I. Lemesh, M. Mawass, Peter. Fischer, M. Kläui, and G. S. D. Beach, Observation of room-temperature magnetic skyrmions and their current-driven dynamics in ultrathin metallic ferromagnets. Nat. Mat. **15**, 501–506 (2016).

[2] X. Yu, W. Koshibae, Y. Tokunaga, K. Shibata, Y. Taguchi, N. Nagaosa, and Y. Tokura, Transformation between meron and skyrmion topological spin textures in a chiral magnet. Nature **564**, 95 (2018).

[3] T. Xu, Y. Ichiki, K. Masuda, Y. Wang, H. Hirakata, and T. J. Shimada, Ultrasmall Polar Skyrmions and Merons in $SrTiO_3$ Heterostructures by Polaron Engineering, ACS Nano **17**, 10836–10843 (2023).

[4] I. Dzyaloshinsky, A thermodynamic theory of "weak" ferromagnetism of antiferromagnetics, J Phys Chem Solids **4**, 241 (1958).

[5] Y. Ga, Q. Cui, Y. Zhu, D. Yu, L. Wang, J. Liang, and H. Yang, Anisotropic Dzyaloshinskii-Moriya interaction protected by D2d crystal symmetry in two-dimensional ternary compounds, npj Comput. Mater. **8**, 128 (2022).

[6] T. Moriya, Anisotropic superexchange interaction and weak ferromagnetism, Phys. Rev. B **120**, 91 (1960).

[7] W. Geng, et al., Real-Time Transformation of Flux-Closure Domains with Superhigh Thermal Stability, Nano Lett. **22**, 8892-8899 (2022).

[8] Y. Tang *et al.*, Observation of a periodic array of flux-closure quadrants in strained ferroelectric PbTiO3 films, Science **348**, 547 (2015).

[9] Z. Hong, S. Das, C. Nelson, A. K. Yadav, Y. Wu, J. Junquera, L.-Q. Chen, L. W. Martin, and R. Ramesh, Vortex domain walls in ferroelectrics, Nano Lett. **21**, 3533 (2021).

[10] T. Shimada, T. Xu, Y. Uratani, J. Wang, and T. Kitamura, Unusual multiferroic phase transitions in PbTiO3 nanowires, Nano Lett. **16**, 6774 (2016).

[11] R. Zhu, Z. Jiang, X. Zhang, X. Zhong, C. Tan, M. Liu, et al., Dynamics of Polar Skyrmion Bubbles under Electric Fields, Phys. Rev. Lett. **129**, 107601 (2022).

[12] L. M. Zhou et al., Local manipulation and topological phase transitions of polar skyrmions, Matter **5**, 1031–1041 (2022)

[13] Y.-T. Shao, et al., Emergent chirality in a polar meron to skyrmion phase transition, Nature Communications **14**, 1355 (2023)

[14] Y. J. Wang, Y. P. Feng, Y. L. Zhu, Y. L. Tang, L. X. Yang, M. J. Zou, W. R. Geng, M. J. Han, X. W. Guo, B. Wu, and X. L. Ma, Polar meron lattice in strained oxide ferroelectrics, Nat. Mater. **19**, 881 (2020).

[15] W. Peng, J. Mun, Q. D. Xie, J. S. Chen, L. F. Wang, M. Kim, and T. W. Noh, Oxygen vacancy-induced topological nanodomains in ultrathin ferroelectric films, npj Quantum Mater. **6**, 48 (2021).

[16] L. Li, X. Cheng, J. R. Jokisaari, P. Gao, J. Britson, C. Adamo, C. Heikes, D. G. Schlom, L.-Q.

Chen, and X. Pan, Defect-Induced Hedgehog Polarization States in Multiferroics, Phys. Rev. Lett. **120**, 137602 (2018).
[17] H. Shang, X. Liang, F. Deng, S. Hu and S. Shen, Flexoelectricity in wrinkled thin films, Int. J. Mech. Sci., **15**, 107685 (2022).
[18] T. Xu, J. Wang, T. Shimada, and T. Kitamura, Direct approach for flexoelectricity from first-principles calculations: Cases for $SrTiO_3$ and $BaTiO_3$, J. Phys.: Condens. Matter **25**, 415901 (2013).
[19] J. Liu, W. Chen, M. Wu, F. Sun, X. Huang, Y. Zheng Bidirectional mechanical switching window in ferroelectric thin films predicted by first-principle-based simulations. Npj Comput. Mater. **8**, 1–9 (2022).
[20] Q. Li, C. T. Nelson, S. L. Hsu, A. R. Damodaran, L. L. Li, A. K. Yadav, M. McCarter, L. W. Martin, R. Ramesh, and S. V. Kalinin, Quantification of Flexoelectricity in $PbTiO_3/SrTiO_3$ Superlattice Polar Vortices Using Machine Learning and Phase-Field Modeling, Nat. Commun. **8**, 1468 (2017).
[21] T. Shimada, Y. Wang, T. Hamaguchi, K. Kasai, K. Masuda, L. V. Lich, T. Xu, J. Wang, and H. Hirakata, Emergence of non-trivial polar topologies hidden in singular stress field in SrTiO3: Topological strain-field engineering, J. Phys. Condens. Matter **33**, 505301 (2021).
[22] G. Dong, et al., Super-elastic ferroelectric single-crystal membrane with continuous electric dipole rotation, Science **366**, 475 (2019).
[23] B. Peng, R.-C. Peng, Y.-Q. Zhang, G. Dong, Z. Zhou, Y. Zhou, T. Li, Z. Liu, Z. Luo, S. Wang et al., Phase transition enhanced superior elasticity in freestanding single-crystalline multiferroic BiFeO3 membranes, Sci. Adv. **6**, eaba5847 (2020).
[24] Y. Zhou, C. Guo, G. Dong, H. Liu, Z. Zhou, B. Niu, D. Wu, T. Li, H. Huang, M. Liu, T. Min, Tip-Induced In-Plane Ferroelectric Superstructure in Zigzag-Wrinkled BaTiO3 Thin Films, Nano Lett. **22**, 2859−2866 (2022).
[25] G. Dong, et al., Periodic Wrinkle-Patterned Single-Crystalline Ferroelectric Oxide Membranes with Enhanced Piezoelectricity. Adv. Mater. **32**, 2004477 (2020).
[26] S. Cai et al., Enhanced polarization and abnormal flexural deformation in bent freestanding perovskite oxides, Nat. Commun. **13**, 5116 (2022).
[27] See Supplemental Material at [URL] for the phase-field simulation method, energetics of single bulge model initialized with non-topological domain configurations, impact of various gradient and flexoelectric coupling coefficients, loading methods, polarization distributions of surface layers, Pontryagin density q, polarization patterns at 300 K, distributions of strain components, strain gradients and flexoelectric field, which includes Refs. [21, 28-36].
[28] L.V. Lich, X. Hou, M.-H. Phan, T.Q. Bui, J. Wang, T. Shimada, T. Kitamura, V.-H. Dinh, Electrocaloric effect enhancement in compositionally graded ferroelectric thin films driven by a needle-to-vortex domain structure transition, J. Phys. D: Appl. Phys. **54**, 255307 (2021).
[29] W. Schranz, A. Tröster, I. Rychetsky, Contributions to polarization and polarization switching in antiphase boundaries of $SrTiO_3$ and $PbZrO_3$, J. Appl. Phys. **128**, 194101 (2020).

[30] H. Unoki and T. Sakudo, Electron Spin Resonance of Fe^{3+} in $SrTiO_3$ with Special Reference to the 110° K Phase Transition, J. Phys. Soc. Jpn. **23**, 546 (1967).
[31] J. Peng, D. Shan, Y. Liu, K. Pan, C. Lei, N. He, Z. Zhang, and Q. Yang, A thermodynamic potential for barium zirconate titanate solid solutions, npj Computational Materials **4**, 66 (2018).
[32] P. Lv, L. Wang, C. S. Lynch, A phenomenological thermodynamic energy function for PIN-PMN-PT relaxor ferroelectric single crystals, Acta Materialia **137**, 93-102 (2017).
[33] Y. Li, S. Choudhury, J. Haeni, M. Biegalski, A. Vasudevarao, A. Sharan, H. Ma, J. Levy, V. Gopalan, and S. Trolier-McKinstry, Phase transitions and domain structures in strained pseudocubic (100) $SrTiO_3$ thin films, Phys. Rev. B **73**, 184112 (2006).
[34] H. Uwe and T. Sakudo, Stress-induced ferroelectricity and soft phonon modes in $SrTiO_3$, Phys. Rev. B **13**, 271 (1976).
[35] P. Zubko, G. Catalan, A. Buckley, P. R. L. Welche, and J. F. Scott, Strain-Gradient-Induced Polarization in $SrTiO_3$ Single Crystals, Phys. Rev. Lett. **99**, 99–102 (2007).
[36] O. Diéguez and M. Stengel, Translational Covariance of Flexoelectricity at Ferroelectric Domain Walls, Phys. Rev. X **12**, 031002 (2022).
[37] F. Xu and M. Potier-Ferry, A multi-scale modeling framework for instabilities of film/substrate systems, J. Mech. Phys. Solids **86**, 150 (2016).
[38] F. Xu, M. Potier-Ferry, S. Belouettar, Y. Cong, 3D finite element modeling for instabilities in thin films on soft substrates, Int. J. Solids Struct. **51**, 3619–3632 (2014).
[39] C. Guo, H. Huang, Design of super-elastic freestanding ferroelectric thin films guided by phase-field simulations, Microstructures, **2**, 2022021 (2022).
[40] Y. Wang, Z. Li, J. Xiao, Stretchable Thin Film Materials: Fabrication, Application, and Mechanics, *J. Electron. Packag*., **138**, 020801 (2016).
[41] Q. Wang, J. Wang, H. Fang, Y. Chen, Y. Han, H. Liu, D. Wang, P. Zhang, C. Shi, J. Guo, B. He, L. Zheng, W. Lü, Polarization Evolution in Morphology-Engineered Freestanding Single-Crystalline $BaTiO_3$ Membranes, J. Phys. Chem. C **126**,16369 (2022).
[42] Y. Han, J. Zhou, H. Wang, L. Gao, S. Feng, K. Cao, Z. Xu, and Y. Lu, Experimental nanomechanics of 2D materials for strain engineering, Appl. Nanosci. **11**, 1075 (2021).
[43] S. Das, B. Wang, T. R. Paudel, S. M. Park, E. Y. Tsymbal, L. Q. Chen, D. Lee, and T. W. Noh, Enhanced flexoelectricity at reduced dimensions revealed by mechanically tunable quantum tunnelling, Nat. Commun. **10**, 537 (2019).
[44] D. Rusu, J. J. P. Peters, T. P. A. Hase, J. A. Gott, G. A. A. Nisbet, J. Strempfer, D. Haskel, S. D. Seddon, R. Beanland, A. M. Sanchez, and M. Alexe, Ferroelectric incommensurate spin crystals, Nature (London) **602**, 240 (2022).
[45] X. Yu, W. Koshibae, Y. Tokunaga, K. Shibata, Y. Taguchi, N. Nagaosa, and Y. Tokura, Nature (London) **564**, 95 (2018).
[46] M. Nelson, J. King, and O. Jensen, Buckling of a growing tissue and the emergence of two-

dimensional patterns, Math. Biosci. **246**, 229 (2013).
[47] G. Dong et al., Self-Assembled Epitaxial Ferroelectric Oxide Nanospring with Super-Scalability, Adv. Mater. **34**, 2108419 (2022).
[48] W. Zhu, T. Low, V. Perebeinos, A. A. Bol, Y. Zhu, H. Yan, J. Tersoff, and P. Avouris, Structure and Electronic Transport in Graphene Wrinkles, Nano Lett. **12**, 3431 (2012).
[49] E. Han, S. M. Nahid, T. Rakib, G. Nolan, P. F. Ferrari, M. A. Hossain, A. Schleife, S. Nam, E. Ertekin, A. M. van der Zande and P. Y. Huang, Bend-induced ferroelectric domain walls in α-In_2Se_3, ACS Nano, **8**, 7881-7888 (2023).
[50] C. Chen, H. Liu, Q. Lai, X. Mao, J. Fu, Z. Fu, and H. Zeng, Large-scale domain engineering in two-dimensional ferroelectric $CuInP_2S_6$, via giant flexoelectric effect, Nano Lett. **22**, 3275 (2022)
[51] M. Guvendiren, J. A. Burdick, and S. Yang, Solvent induced transition from wrinkles to creases in thin film gels with depth-wise crosslinking gradients, Soft Matter **6**, 5795 (2010).
[52] Y. Tan, B. Hu, J. Song, Z. Chu, and W. Wu, Bioinspired multiscale wrinkling patterns on curved substrates: An overview, Nano-Micro Lett. **12**, 1 (2020).
[53] X. Zhuang, B. He, B. Javvaji, and H. S. Park, Intrinsic bending flexoelectric constants in two-dimensional materials, Phys. Rev. B **99**, 054105 (2019).
[54] W. Shi, Y. Guo, Z. Zhang, and W. Guo, Flexoelectricity in monolayer transition metal dichalcogenides, J. Phys. Chem. Lett. **9**, 6841 (2018).
[55] C. Chen, H. Liu, Q. Lai, X. Mao, J. Fu, Z. Fu, and H. Zeng, Large-scale domain engineering in two-dimensional ferroelectric $CuInP_2S_6$ via giant flexoelectric effect, Nano Lett. **22**, 3275 (2022).

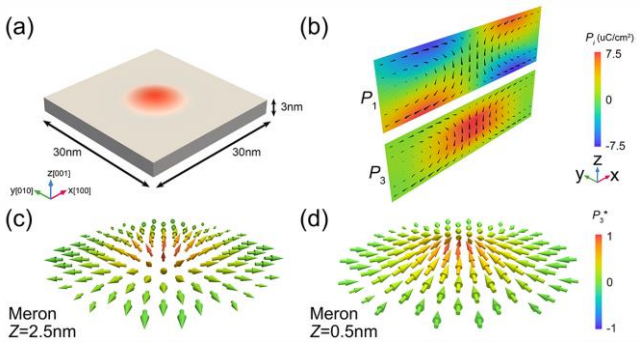

Figure 1. Ferroelectric properties in the $SrTiO_3$ nanofilm with a single bulge at 273 K. (a) The simulation nanofilm with a bulge in the center (red part). (b) Distribution of P_1 and P_3 within the *x*-*z* plane across the bulge; The arrows denote polarization vectors and the color indicates the values of P_1 (along *x* direction) and P_3 (along *z* direction) components. (c)(d) Polarization patterns in the subtop and subbottom layers within the bulge.

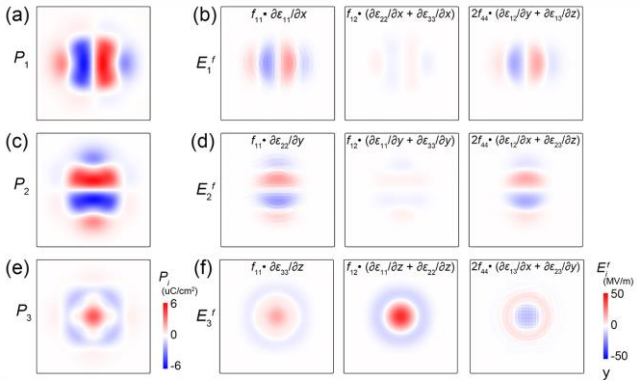

Figure 2. (a), (c) and (e) Polarization components in the subtop layer (Z = 2.5 nm). (b), (d) and (f) Distribution of the flexoelectric fields generated by different strain gradients.

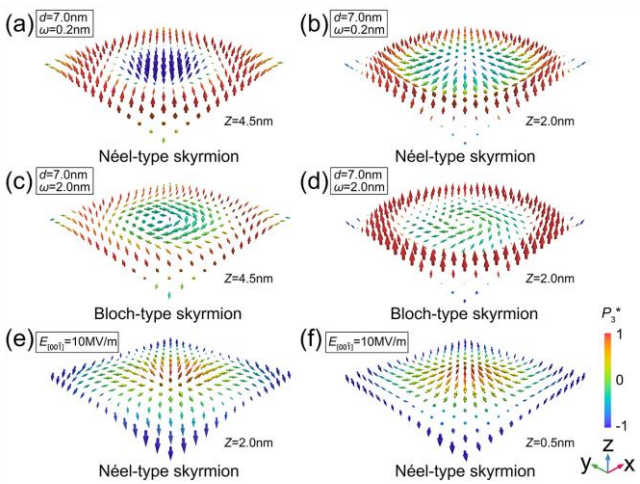

Figure 3. Polar textures in the inner layers of rippled $SrTiO_3$ nanofilm with different geometries and electric boundary conditions. (a)(b) d = 7 nm, ω = 0.2 nm; (c)(d) d = 7 nm, ω = 2 nm; (e)(f) d = 3 nm, ω= 0.2 nm under external electric field of 10 MV/m along $[00\bar{1}]$.

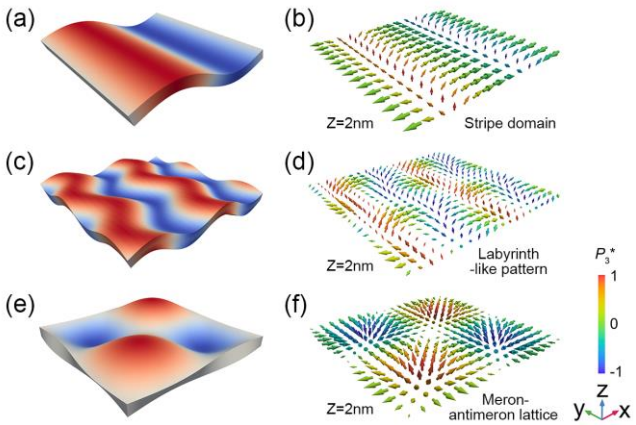

Figure 4. Ferroelectric patterns in the $SrTiO_3$ nanofilm with (a)(b)1D sinusoidal, (c)(d)2D herringbone and (e)(f) checkerboard deformations.